Journal of Solid State Chemistry 182 (2009) 2475–2485

Contents lists available at ScienceDirect

Journal of Solid State Chemistry

journal homepage: www.elsevier.com/locate/jssc

General and facile synthesis of ceria-based solid solution nanocrystals and their catalytic properties

Huan-Ping Zhou [a], Rui Si [a], Wei-Guo Song [b], Chun-Hua Yan [a,*]

[a] Beijing National Laboratory for Molecular Sciences, State Key Laboratory of Rare Earth Materials Chemistry and Applications, PKU-HKU Joint Laboratory in Rare Earth Materials and Bioinorganic Chemistry, Peking University, Beijing 100871, China

[b] Beijing National Laboratory for Molecular Sciences, Institute of Chemistry, Chinese Academy of Sciences, Beijing 100080, China

ARTICLE INFO

Article history:
Received 23 April 2009
Received in revised form
1 July 2009
Accepted 2 July 2009
Available online 8 July 2009

Keywords:
Solid solutions
Ultra-small nanocrystals
Ceria-based material
Catalytic property

ABSTRACT

Uniform $Ce_{1-x}Zr_xO_2$ ($x = 0.2$–0.8) nanocrystals with ultra-small size were synthesized through a thermolysis process, facilitated by the initial formation of precursor (hydrated (Ce,Zr)-hydroxides) at low temperature. TEM, XRD, EDAX, and Raman spectra were employed to study the formation of the solid solutions with various Ce/Zr ratios. Ultraviolet–visible (UV–vis) spectra showed that the ratios of Ce^{3+} to Ce^{4+} in both surface and bulk for the as-prepared $Ce_{1-x}Zr_xO_2$ nanocrystals increased with the zirconium content x. The well-distributed Zr and Ce in the hydrated (Ce,Zr)-hydroxides before their thermolysis became the crucial factor for the structural homogeneity of the products. In addition, this strategy was extended to the synthesis of $Ce_{1-x}Gd_xO_{1-x/2}$, $Ce_{1-x}Sm_xO_{1-x/2}$, and $Ce_{1-x}Sn_xO_2$ solid solutions. Catalytic measurements indicated that the ceria-based catalysts were active for CO oxidation at temperatures beyond 250 °C and the sequence of catalytic activity was $Ce_{0.5}Zr_{0.5}O_2 > Ce_{0.8}Zr_{0.2}O_2 > Ce_{0.2}Zr_{0.8}O_2 > Ce_{0.5}Sm_{0.5}O_{1.75}$.

1. Introduction

The modernization in most countries is accompanied with the development of factories and automobiles, which further swamps into a dilemma of energy crisis and environment pollution. The rapid improvement of excellent catalytic materials, however, active recently in fields such as oil cracking and controlling of automobile emission, becomes one of the promising solutions of these exacerbating energy and environmental problems. In this respect, ceria (CeO_2), one of the most important functional rare-earth oxides, and ceria-based materials are of great significance and hold intensive interest for researchers because of their successful applications as automotive three-way catalysts (TWCs), as well as ultraviolet (UV) absorbers, solid oxide fuel cells (SOFCs), and glass-polishing materials [1–17]. Since 1995, CeO_2–ZrO_2 mixed oxides have gradually replaced pure CeO_2 as oxygen storage capacity (OSC) materials in the TWCs to reduce the emission of toxic pollutants (CO, NO_x, hydrocarbons, etc.) from automobile exhaust, due to their enhanced reduction behavior and improved thermal stability at elevated temperatures [3,11,12]. CeO_2–Sm_2O_3 and CeO_2–Gd_2O_3 also show application potential in the next generation of compact SOFCs because of their high ionic conductivity coupled with low activation energy for ionic conduction [13,14]. Moreover, CeO_2–SnO_2 solid solutions are important catalysts for their superior redox efficiency at low temperature [15].

So far, numerous technical routes including ball milling, co-precipitation, sol–gel, and hydrothermal processes have been developed to prepare ceria-based materials [16–23]. However, these approaches provide limited control over the chemical composition, crystalline phase, and grain size of the resultant nanoparticles. For example, although the precipitation method can tailor the chemical composition of the CeO_2–ZrO_2 solid solution, the as-prepared nanocrystals can easily form aggregates, which cannot re-disperse in any solvent [23,24]. Meeyoo et al. synthesized nanostructured $Ce_{1-x}Zr_xO_2$ ($x = 0.2$–0.8) via a urea hydrolysis process and the as-obtained $Ce_{1-x}Zr_xO_2$ nanoparticles were somewhat nonhomogeneous in terms of microdomain and phase segregation [25]. To obtain the CeO_2–ZrO_2 mixed oxides with better textural stability and redox property, a number of research groups have been involved in synthesizing CeO_2–ZrO_2 solid solutions with high stoichiometric proportion and structural homogeneity [12,26]. Our group also studied the preparation and catalytic behavior of the CeO_2–ZrO_2 mixed oxides with homogeneous textural and uniform size [4]. However, the controlled synthesis of other ceria-based materials, such as CeO_2–Sm_2O_3, CeO_2–Gd_2O_3, and CeO_2–SnO_2, is still insufficient [27–29]. Recently, the non-aqueous synthetic routes, such as thermal decomposition of metal-surfactant complex in high-boiling point solvents, have proved to be effective in preparing monodispersed

* Corresponding author. Fax: +86 10 6275 4179.
E-mail address: yan@pku.edu.cn (C.-H. Yan).

0022-4596/$ - see front matter © 2009 Elsevier Inc. All rights reserved.
doi:10.1016/j.jssc.2009.07.002

CeO_2 and ZrO_2 nanoparticles [31–36]. However, the non-aqueous routes are difficult to synthesize ceria-based composite oxides of high quality due to the limitation in manipulation of hetero-metal reactants. Therefore, the development of a facile and general method for synthesizing high-quality ceria-based nanocrystals with homogenous structure, high stoichiometric proportion, and uniform size and morphology holds a great challenge for the current investigation.

In this article, a modified thermolysis method was employed for the synthesis of the rare-earth-based nanocrystals. Taking CeO_2–ZrO_2 as a typical example, the nanoparticles with small size and uniform shape were acquired under proper condition, facilitated by the initial formation of precursor (hydrated (Ce,Zr)-hydroxides) at low temperature. Transmission electron microscopy (TEM), powder X-ray diffraction (PXRD), energy dispersive X-ray analysis (EDAX), and Raman spectra, etc. served as effective tools to study the formation of solid solutions with various Ce/Zr ratios. In addition, this strategy was extended to the synthesis of homogeneous texture solid solutions of CeO_2–Sm_2O_3, CeO_2–Gd_2O_3, and CeO_2–SnO_2. This facile method can be applied to synthesize other solid solution nanocrystals with ultra-small size and uniform morphology.

2. Experimental section

2.1. Chemicals and materials

Oleic acid (OA, Aldrich), oleylamine (OM, Acros), 1-octadecene (ODE, Acros), ceric ammonium nitrate ($(NH_4)_2Ce(NO_3)_6$, Sigma-Aldrich, $\geq$99.5%), $ZrO(NO_3)_2$ (AR, $\geq$97.8%), $Sm(NO_3)_3$ (AR, $\geq$99.0%), $SmCl_3$ (AR, $\geq$99.0%), $Gd(NO_3)_3$ (AR, $\geq$99.0%), $SnCl_4$ (AR, $\geq$99.0%), NH_4OH (AR), ethanol (AR), and cyclohexane (AR) were used as received without further purification.

2.2. Preparation

2.2.1. Synthesis of $Ce_{1-x}Zr_xO_2$ nanocrystals

Typically, (Ce,Zr)-hydroxides were precipitated by the reaction between $(NH_4)_2Ce(NO_3)_6$, $ZrO(NO_3)_2$ and ammonia. Then the as-prepared precipitate was added to the mixture of OA and OM with proper ratio in a three-necked flask at room temperature. The slurry was heated to 140 °C to remove water and oxygen for 30 min, and thus to form an optically transparent solution. After that, the resulting mixture was heated to 300–330 °C at a heating rate of 12 °C/min, and was kept at this temperature for 0.5–1 h under Ar atmosphere. Then, an excess amount of ethanol was poured into the solution at room temperature. The resultant mixture was centrifugally separated and the products were collected. The as-precipitated nanocrystals were washed several times with ethanol and then dried in air at 70 °C overnight. The yields of all the obtained nanocrystals were around 80%. The as-prepared nanocrystals could be easily redispersed in various non-polar organic solvents, such as cyclohexane and toluene.

2.2.2. Synthesis of $Ce_{1-x}Gd_xO_{1-x/2}$, $Ce_{1-x}Sm_xO_{1-x/2}$, and $Ce_{1-x}Sn_xO_2$ Nanocrystals

The synthetic strategy was similar to that of $Ce_{1-x}Zr_xO_2$, except that the precursors were substituted by (Ce,Gd)-hydroxides, (Ce,Sm)-hydroxides, and (Ce,Sn)-hydroxides, which were obtained by the reaction between the pairs of $(NH_4)_2Ce(NO_3)_6$ and $Gd(NO_3)_3$, $(NH_4)_2Ce(NO_3)_6$ and $Sm(NO_3)_3$ or $SmCl_3$, $(NH_4)_2Ce(NO_3)_6$ and $SnCl_4$ in the ammonia solution.

2.2.3. Synthesis of $Pt/Ce_{0.5}Zr_{0.5}O_2$

Platinum particles were synthesized according to literature methods [30]. A total of 100 mg of Poly(*N*-vinyl-2-pyrrolidone) (PVP, Mw = 30,000) was dissolved in a mixture of 5 mL of 6.0 mM $H_2PtCl_6 \cdot 6H_2O$ aqueous solution, 40 mL of methanol and 5 mL of water. The mixture was refluxed for 3 h. The solvent was evaporated, and the residue was redispersed in water. 0.07 g of the calcined $Ce_{0.5}Zr_{0.5}O_2$ was added to Pt colloidal aqueous solution, and the slurry was refluxed for 5 h at room temperature. The precipitates were separated by centrifugation, washed with water, and dried in an oven at 100 °C and then were calcined at 400 °C for 4 h in air.

2.3. Characterization

Powder X-ray diffraction (PXRD) patterns of the dried powders were recorded on a Rigaku D/MAX-2000 diffractometer (Japan) with a slit of 1/2° at a scanning rate of 2° min^{-1}, using Cu K_α radiation ($\lambda = 1.5406$ Å). The lattice parameters were calculated with the least-squares method. Samples for transmission electron microscopy (TEM) analysis were prepared by drying a nanocrystal dispersion in hexane on amorphous carbon-coated copper grids. Particle sizes and shapes were examined by a TEM (200CX, Jeol, Japan) operated at 160 kV. High-resolution TEM (HRTEM) characterization was performed with a Philips Tecnai F30 FEG-TEM operated at 300 kV. The BET specific surface area (S_{BET}) was measured by nitrogen adsorption at 78.3 K, using an ASAP 2010 analyzer (Micromeritics Co. Ltd.), and measurements were performed after outgassing the sample at 423 K for 4 h under a vacuum, down to a residual pressure better than 10^{-3} Torr. The laser Raman spectra were recorded using a Jobin–Yvon HR800 Raman spectrometer with a 30 mW Ar ion laser (488.0 nm). The UV–vis spectra of the nanocrystals dispersions were recorded on a HITACHI U-3010 spectrometer using a quartz cell (1 cm path length), and pure hexane was used as a blank.

2.4. CO oxidization test

A home-made flow reactor system including a quartz reaction tube (8 mm × 42 mm) was used for the catalytic test. In a typical CO oxidation experiment, 50 mg as-calcined ceria-based nanocrystals and 500 mg sea sand were mixed as a catalyst, and the experiment was carried out under the flow of the reactant gas mixture (0.5% CO, 10% O_2, balanced with N_2) at a rate of 50 mL min^{-1}. The composition of gas was monitored on-line by gas chromatography (Shimadzu, GC-14C).

3. Results and discussion

3.1. Characterization of CeO_2–ZrO_2 solid solutions

3.1.1. TEM

Fig. 1 shows the typical TEM micrographs of the as-prepared $Ce_{1-x}Zr_xO_2$ ($x = 0.2$–0.8) nanocrystals. Compared with the products acquired from hydrolysis process [4], the nanocrystals retained a polyhedron shape, but differed in their ultra-small size and narrow size distribution. The particle sizes *D* detected from TEM for the $Ce_{1-x}Zr_xO_2$ ($x = 0.2$–0.8) samples are listed in Table 1, with 4.2 nm ± 0.8 nm, 3.9 nm ± 0.6 nm, 5.0 nm ± 0.7 nm, 3.8 nm ± 0.6 nm, 5.1 nm ± 0.6 nm, for *x* increased from 0.2 to 0.8. The lattice fringes with the interplanar spacing of 0.32, 0.32, and 0.28 nm, shown in the insets of Fig. 1a, c, and e, are determined to be associated with the {1 1 1} facets of $Ce_{0.2}Zr_{0.8}O_2$ (Fig. 1a), {1 1 1} facets of $Ce_{0.5}Zr_{0.5}O_2$ (Fig. 1c), and {1 0 1} facets of $Ce_{0.2}Zr_{0.8}O_2$

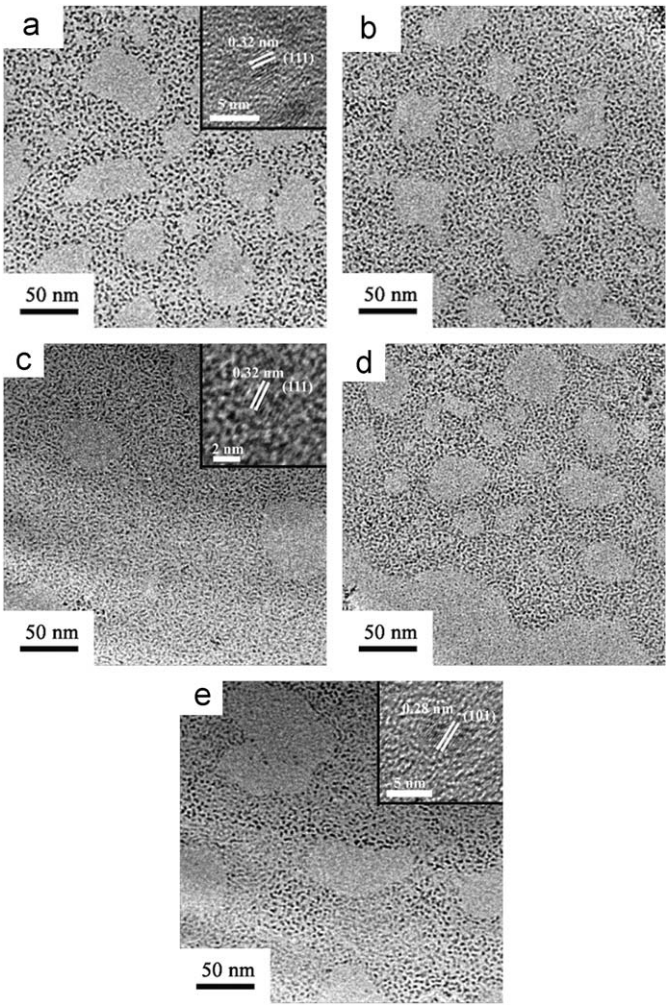

Fig. 1. TEM images of the as-prepared $Ce_{1-x}Zr_xO_2$ ($x = 0.2$–0.8) nanocrystals. (a) $x = 0.2$, 1 mmol (Ce,Zr)-hydroxides, OA/OM = 1:3, 330 °C, 0.5 h; (b) $x = 0.4$, 1 mmol (Ce,Zr)-hydroxides, OA/OM = 2:3, 300 °C, 0.5 h; (c) $x = 0.5$, 1 mmol (Ce,Zr)-hydroxides, OA/OM = 2:3, 300 °C, 0.5 h; (d) $x = 0.6$, 1 mmol (Ce,Zr)-hydroxides, OA/OM = 1:3, 300 °C, 0.5 h; (e) $x = 0.8$, 1 mmol (Ce,Zr)-hydroxides, OA/OM = 2:3, 300 °C, 0.5 h.

(Fig. 1e), respectively, showing that the CeO_2–ZrO_2 products were well crystallized through the thermolysis treatment.

3.1.2. UV–vis spectra

Fig. 2 shows the UV–vis absorption spectra of the as-obtained $Ce_{1-x}Zr_xO_2$ ($x = 0.2$–0.8) samples. It is reported that polycrystalline ceria and tetragonal zirconia have strong absorption in the UV region with the absorption threshold near 400 and 240 nm, respectively [37,38]. However, the present $Ce_{1-x}Zr_xO_2$ nanocrystals showed absorption bands at ca. 286 and 233 nm. It is well documented that the absolute absorbance coefficient α in these wavelength ranges is generally in proportion to the cerium content $1-x$. Thus, the above bands at ca. 286 and 233 nm wavelength can be attributed to the $O^{2-} \rightarrow Ce^{4+}$ and $O^{2-} \rightarrow Ce^{3+}$ charge transfer (CT) transitions, respectively. Compared with the bands at 300 nm ($O^{2-} \rightarrow Ce^{4+}$) and 260 nm ($O^{2-} \rightarrow Ce^{3+}$) reported by our group [4], we suggested that this blue shift might result from the ultra-small size of the present nanocrystals. From Fig. 2, it is noted that the absorption ratio of CT ($O^{2-} \rightarrow Ce^{3+}$) to CT ($O^{2-} \rightarrow Ce^{4+}$) increased with x, evincing that the bulk ratio of Ce^{3+} to Ce^{4+} in the $Ce_{1-x}Zr_xO_2$ nanocrystals increases with doping ZrO_2. The increase of both surface and bulk ratios of Ce^{3+} to Ce^{4+} is probably because the insertion of the smaller Zr^{4+} ion ($r_{Zr(IV)} = 0.84$ Å) can partially compensate for the expansion of the crystal lattice deriving from the transformation of the Ce^{4+} ion ($r_{Ce(IV)}$ 0.97 Å) to the larger Ce^{3+} ion ($r_{Ce(III)} = 1.10$ Å). Furthermore, it can be found that with the similar doping content of Zr^{4+} ion, the surface and bulk ratios of Ce^{3+} to Ce^{4+} in these ultra-small nanocrystals are largely enhanced, when compared with the $Ce_{1-x}Zr_xO_2$ nanocrystals prepared by the urea-based hydrothermal method reported by our group [4].

3.1.3. Raman spectra and PXRD

As is well known, the CeO_2–ZrO_2 mixed oxides have a quite complex phase diagram, containing three stable phases (monoclinic (m), tetragonal (t), and cubic (c)) and two metastable phases (t', t''). Among the above three tetragonal phases (t, t', t''), the t phase is formed through a diffused phase decomposition, while the t' phase with the same space group of $P4_2/nmc$ is obtained through a diffusionless transition, and the pseudo-cubic t'' phase with a space group of $P4_2/nmc$ is an intermediate phase between t' and cubic CeO_2, very close to the fluorite cubic structure except

Table 1
The synthesis condition, size and EDAX results for the as-prepared nanocrystals.

	x precursor		OA:OM	T (°C)	t (min)	size (nm)	EDAX x (mol%)
$Ce_{1-x}Zr_xO_2$	0.2	(Ce,Zr)-hydroxides prepared from $(NH_4)_2Ce(NO_3)_6$ and $ZrO(NO_3)_2$	1:3	330	30	4.2 ± 0.8[a]	19.6
	0.4		2:3	300	30	3.9 ± 0.6	
	0.5		2:3	300	30	5.0 ± 0.7	53.9
	0.6		1:3	300	30	3.8 ± 0.6	
	0.8		2:3	300	30	5.1 ± 0.6	87.6
$Ce_{1-x}Gd_xO_{1-x/2}$	0.2	(Ce,Gd)-hydroxides prepared from $(NH_4)_2Ce(NO_3)_6$ and $Gd(NO_3)_3$	2:3	300	60	4.4 ± 0.6	
	0.5		2:3	300	30	3.2 ± 0.4	48.6
	0.8		1:3	300	60		
$Ce_{1-x}Sm_xO_{1-x/2}$	0.2	(Ce,Sm)-hydroxides prepared from $(NH_4)_2Ce(NO_3)_6$ and $Sm(NO_3)_3$	2:3	300	60	3.6 ± 0.3	
	0.5		1:3	300	60	3.2 ± 0.6	47.3
	0.8		1:3	300	60		
$Ce_{1-x}Sm_xO_{1-x/2}$	0.5	(Ce,Sm)-hydroxides prepared from $(NH_4)_2Ce(NO_3)_6$ and $SmCl_3$	2:3	300	60	12.4 ± 1.0	51.3
$Ce_{1-x}Sn_xO_2$	0.2	(Ce,Sn)-hydroxides prepared from $(NH_4)_2Ce(NO_3)_6$ and $SnCl_4$	1:3	300	30	3.3 ± 0.6	22.3
	0.5		2:3	300	30	3.0 ± 0.4	
	0.8		2:3	300	30		

[a] The standard deviation statistic from 100 nanocrystals.

that there exists the displacement of the oxygen atom in its crystal lattice [39–42]. Fig. 3a shows the PXRD patterns of the as-prepared $Ce_{1-x}Zr_xO_2$ ($x = 0.2$–0.8) nanocrystals. The broad

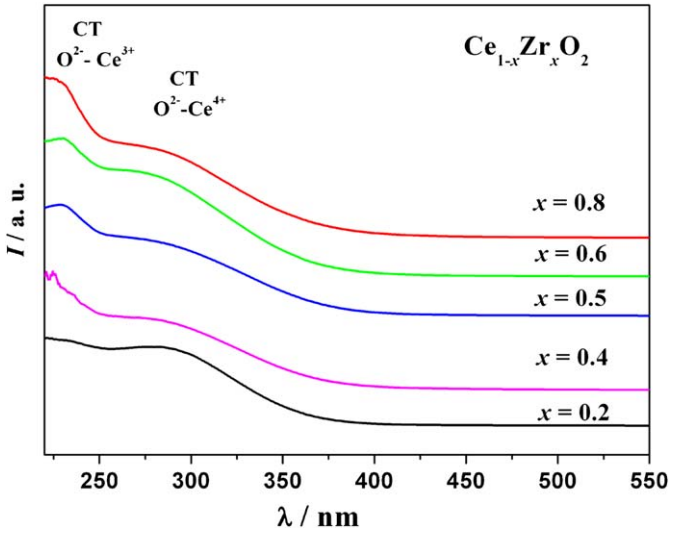

Fig. 2. UV–vis absorption for the as-prepared $Ce_{1-x}Zr_xO_2$ ($x = 0.2$–0.8) nanocrystals.

reflections in the diffractograms attributed to their ultra-small size impede the accurate analysis of the crystal structures of the present samples through PXRD. Therefore, Raman spectroscopy combined with PXRD served as an effective tool for detecting the crystal structure of the CeO_2–ZrO_2 samples. Fig. 3b is the vis–Raman spectra of the as-prepared $Ce_{1-x}Zr_xO_2$ nanocrystals. For $Ce_{0.2}Zr_{0.8}O_2$ three Raman peaks at 152, 271, and 627 cm^{-1} and three weak bands at ca. 315, 471 and 550 cm^{-1}, originating from the six Raman active modes (A_{1g} +$2B_{1g}$+$3E_g$) of t-ZrO_2, could be located [43–45]. When $x = 0.5$–0.6, the apparent similar intensity of Raman peak at 461–468 cm^{-1} (F_{2g} mode of c-CeO_2) and at 627 cm^{-1}, combined with the peaks appearing at 152 and 315 cm^{-1}, indicate a metastable phase (t'') in CeO_2–ZrO_2 materials [41]. While for $x = 0.2$–0.4, the $Ce_{1-x}Zr_xO_2$ samples showed one strong Raman peak at 461–468 cm^{-1} (F_{2g} mode of c-CeO_2) and three weak bands at ca. 152, 271, and 627 cm^{-1}, attributed to the presence of defective structure in the CeO_2–ZrO_2 materials [41]. It is reported that f–f transitions can influence the Raman spectra as well as promote surface area thermal stability or catalytic activity [46]. Moreover, the lanthanide ions present as impurities can be considered as useful spectroscopic probes of the site symmetry of the metal ions [46]. In our case, the Raman spectra were also used to confirm the structure of the solid solutions. Due to the high purity of the reagents we used, no pronounced influence arising from the impurities has been observed.

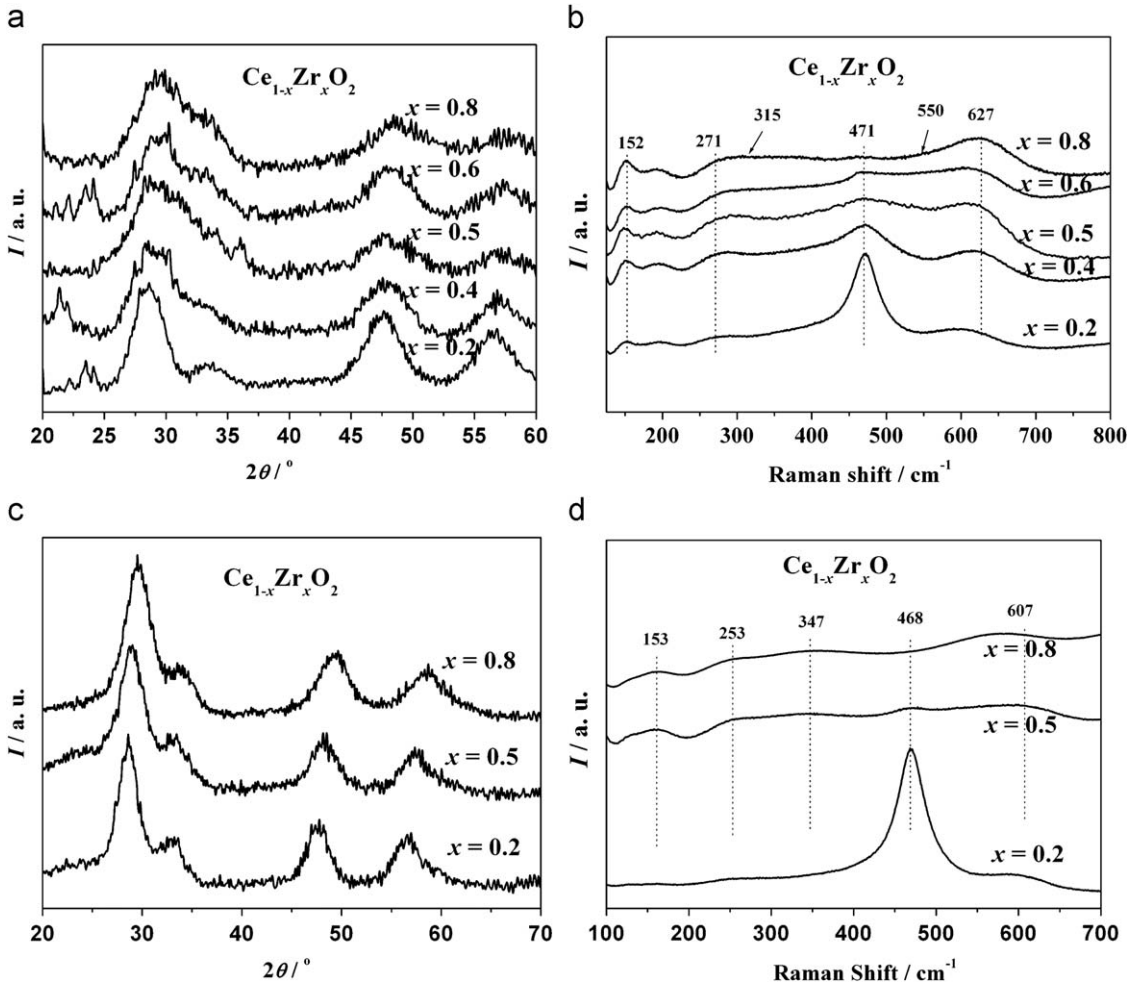

Fig. 3. (a) PXRD patterns and (b) Raman spectra of the as-prepared $Ce_{1-x}Zr_xO_2$ ($x = 0.2$–0.8) nanocrystals; (c) PXRD pattern and (d) Raman spectrum of the $Ce_{1-x}Zr_xO_2$ ($x = 0.2$, 0.5, 0.8) nanocrystals after calcinations at 400 °C for 4 h.

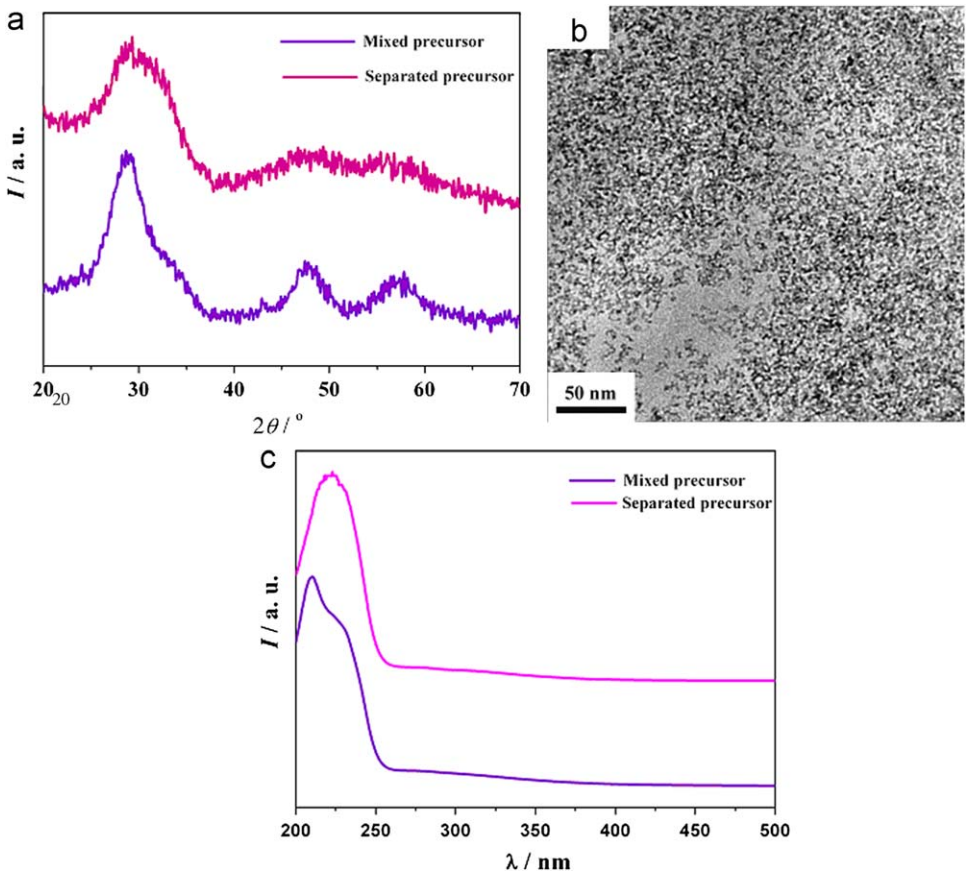

Fig. 4. (a) PXRD pattern and (b) TEM images of the as-prepared $Ce_{0.5}Zr_{0.5}O_2$ nanocrystals, with separate cerium-hydrate and zirconium-hydrate as the precursors; (c) UV–vis absorption for the (Ce,Zr)-hydroxides and the mixture (Ce-hydroxides mixed with Zr-hydroxides) dissolved in the solution of OA and OM.

Fig. 3c and d show the PXRD patterns and Raman spectra of the $Ce_{1-x}Zr_xO_2$ ($x = 0.2, 0.5, 0.8$) samples calcined at 400 °C. The PXRD and Raman peaks are stronger, but still broad, indicating the as-calcined $Ce_{1-x}Zr_xO_2$ samples have an ultra-small size. The particle sizes D calculated from PXRD for the $Ce_{1-x}Zr_xO_2$ ($x = 0.2$, 0.5, and 0.8) powders were 3.3, 2.9, and 2.4 nm, respectively, quite different from those detected by TEM. The combination of Raman spectra (Fig. 3d) and PXRD showed that the as-calcined $Ce_{0.8}Zr_{0.2}O_2$ and $Ce_{0.2}Zr_{0.8}O_2$ samples confirmed cubic and stable tetragonal (t) structures, respectively. The disappearance of the weak bands at ca. 152 cm^{-1} for $Ce_{0.8}Zr_{0.2}O_2$ implied that the sintering process to some extent attenuated the defects in its crystal lattice. $Ce_{0.8}Zr_{0.2}O_2$ has a fluorite cubic structure with lattice parameter $a = 5.4064(0)$ Å (JCPDS card no. 34–394) and $Ce_{0.2}Zr_{0.8}O_2$ is a stable t phase with the lattice parameters of $a = 5.1081(8)$ Å and $c = 5.3860(5)$ Å, to be compared with the polycrystalline $Ce_{0.2}Zr_{0.8}O_2$ sample reported by Kašpar et al. with the Rietveld refinement method ($a = 5.1516$ Å, $c = 5.2405$ Å) [47]. For $x = 0.5$, the as-calcined $Ce_{1-x}Zr_xO_2$ powders showed a metastable phase (t''), based on their Raman bands lying at ca. 153, 253, 347, 468, and 607 cm^{-1}. Consistant with the Raman spectra, the $Ce_{0.5}Zr_{0.5}O_2$ samples showed a metastable t structure with lattice parameters of 5.3225(4) Å.

3.2. Controllable synthesis of CeO_2–ZrO_2 solid solutions

Recently, the preparation of single-phase CeO_2–ZrO_2 solid solutions has attracted much of researchers' interest, due to their better textural property, thermal stability, and redox behaviors compared with microdomain- or phase-segregated nonhomogeneous ones [12,26]. For example, Meeyoo et al. synthesized nanostructured $Ce_{1-x}Zr_xO_2$ mixed oxides via the hydrolysis-based co-precipitation with $Ce(NO_3)_3$ and urea, while the as-derived products with $x > 0.5$ appeared somewhat phase segregated when calcinated at 773 K [25]. The recent work presented by our group has shown that homogeneous $Ce_{1-x}Zr_xO_2$ nanomaterials with high thermal stability up to 1273 K can be obtained through hydrothermal strategy, indicating the well-dispersed Zr and Ce in the hydrated (Ce,Zr)-hydroxides before their thermolysis might be the crucial factor for the structural homogeneity of the products [4].

Non-aqueous thermolysis process as the general and versatile method has been used for the synthesis of a variety of high-quality nanocrystals. Recent works show the evidence that this robust synthesis method provides convenience for the formation of CeO_2 and ZrO_2, respectively [31–36]. For instance, the ceria nanocrystals including cubes and ployhedra can be acquired via thermolysis process, using the $Ce(NO_3)_3$, $(NH_4)_2Ce(NO_3)_6$, $Ce(acac)_4$, or $Ce(HBA)_4$ as the starting materials [31–33,36]; similarly, zirconium isopropoxide isopropanol and $ZrCl_4$ are the popular precursors for the preparation of uniform ZrO_2 nanocrystals [34,35]. In addition, the recent work reported by our group has pointed out that the formation of rare-earth nanocrystals is not contingent on the types of rare-earth precursors [48,49]. Therefore, the present synthesis strategy, which employs homogenous hydrolysis at low temperature, then the thermolysis of the hydrated (Ce,Zr)-hydroxides at high temperature, is expected to enable the formation of Ce–Zr solid solution with structural homogeneity and high quality.

The whole synthesis process can be described in the following steps: (1) Initial formation of hydrated (Ce,Zr)-hydroxides: NH_4OH

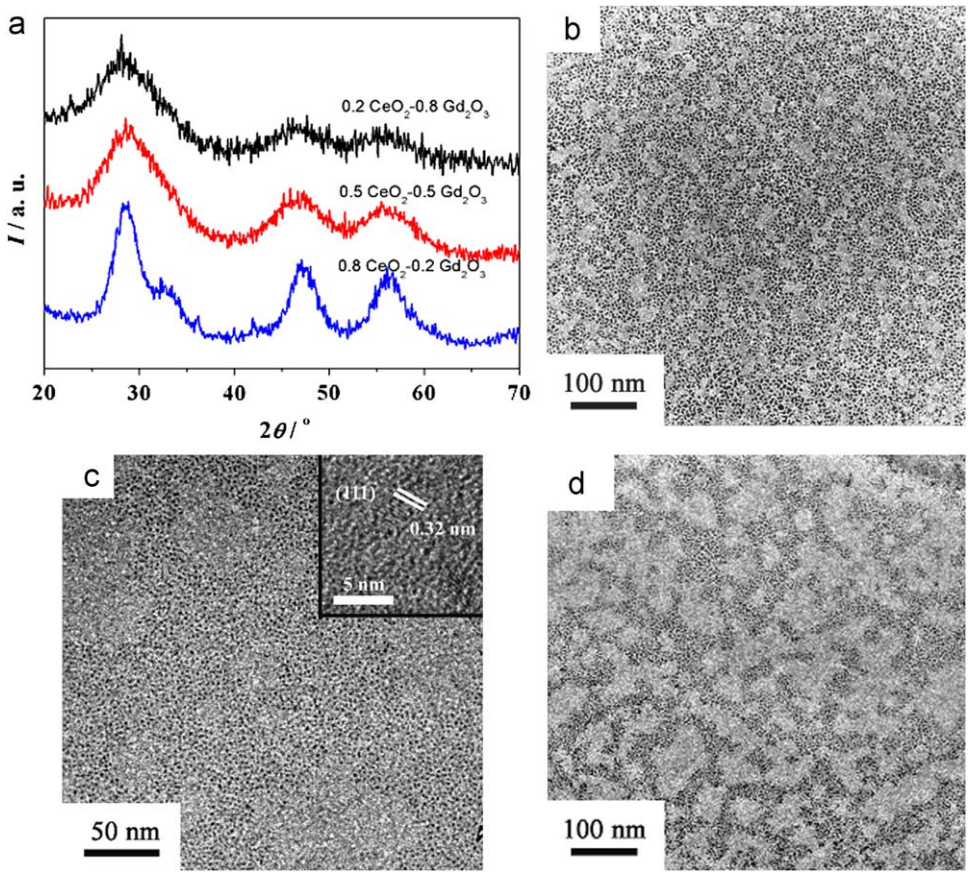

Fig. 5. (a) PXRD of the as-prepared $Ce_{1-x}Gd_xO_{1-x/2}$ ($x = 0.2$, 0.5, 0.8) nanocrystals. TEM images of the as-prepared $Ce_{1-x}Gd_xO_{1-x/2}$ ($x = 0.2$, 0.5, 0.8) nanocrystals: (b) $x = 0.2$, 1 mmol (Ce,Gd)-hydroxides, OA/OM = 2:3, 300 °C, 1 h; (c) $x = 0.5$, 1 mmol (Ce,Gd)-hydroxides, OA/OM = 2:3, 300 °C, 0.5 h; (d) $x = 0.8$, 1 mmol (Ce,Gd)-hydroxides, OA/OM = 1:3, 300 °C, 1 h.

is used as the base source to produce OH^- to control the hydrolysis. The hydrolysate mixtures are then stirred for several hours to ensure the homogenous hydrolysis, that is, the $[Ce(OH)_m(H_2O_n)]^{4-m}$ and $[Zr(OH)_p(H_2O)_q]^{4-p}$ form, integrate and transform into hydrated (Ce,Zr)-hydroxides ($[(Ce_{1-x}Zr_x)(OH)_y(H_2O)_z]^{4-y}$), where $m+n$ and $p+q$ denote the coordination numbers of the metal ions, facilitating the following transformation from hydrated (Ce,Zr)-hydroxides to CeO_2–ZrO_2 nanocrystals through thermolysis process [50]. (2) Formation of $(Ce,Zr)L_{4-x}(RCOO)_x$: The metal source compound ($(Ce,Zr)L_4$, $L = OH^-$) is fully dissolved in a long-chain fatty acid (RCOOH) solution upon heating to a certain temperature, in which L^- ions are substituted by $RCOO^-$. (3) The decomposition of $(Ce,Zr)L_{3-x}(RCOO)_x$ takes place on further elevated temperature, resulting in the formation of $(Ce,Zr)O_2$. During the formation process, the cation-exchange reaction between Ce^{4+} and Zr^{4+} achieves a well-maintained balance between nucleation and growth stages, which would probably facilitate the formation of solid solutions, consistant with a process named Limited Anion-Exchange Reaction for the synthesis of compounds including $REPO_4^{3-}$ and $REVO_4^{3-}$, etc. [49].

A series of CeO_2–ZrO_2 solid-solution nanocrystals for $x = 0.2$–0.8 were obtained by manipulating several parameters such as the ratio of OA/OM, temperature and time. We speculated OA and OM to be the most normal capping agents, whose ratio can be regarded as the crucial reaction parameter to achieve the formation of high-quality nanoparticles. Also, the relative high temperature and proper reaction time contribute to the composition and phase homogeneity. The proper ratio of OA/OM for the synthesis of CeO_2–ZrO_2 solid solution is 1/3 or 2/3. While the temperature is set at 300 or 330 °C, for the appearance of color change and for large bubbles to occur the temperature range should be from 220 to 260 °C, which suggests the growth of the product; thus, a higher temperature promotes high crystallinity.

It is very important to find the main factors determining the formation of the present CeO_2–ZrO_2 solid solution with high dopant concentrations, compared with the results of lower dopant concentrations via other synthesis strategy [17]. Two different ways for the preparation of the precursors are therefore compared, that is, the separate hydrolysis of Ce precursors and Zr precursors, forming $[Ce(OH)_m(H_2O_n)]^{4-m}$ and $[Zr(OH)_p(H_2O)_q]^{4-p}$ respectively, and their simultaneous hydrolysis, resulting in the complex hydrated (Ce,Zr)-hydroxide, $[(Ce_{1-x}Zr_x)(OH)_y(H_2O)_z]^{4-y}$. Taking the synthesis of the nanocrystals $Ce_{1-x}Zr_xO_2$ with $x = 0.5$ as an example, we obtained two kinds of products via different treating processes for the preparation of the precursors, ensuring the same reaction condition in the thermolysis stage. Fig. 4a,b showed the PXRD and TEM images for the nanocrystals acquired through the separate cerium-hydrate and zirconium-hydrate precursors. The as-prepared nanocrystals were somewhat phase segregated (Fig. 4a) and slightly agglomerate (Fig. 4b), according to the EDAX results of the nonhomogenous composition ratio, the ratio of Ce/Zr, which is not fixed at 1:1, but changed in different regions. Herein, UV–vis spectra represents an effective tool to illustrate states of Ce^{4+} and Zr^{4+} ions in the precursors obtained in different ways, portraying the different absorption bands between the (Ce,Zr)-hydroxides and the mixture (Ce-hydroxides mixed with Zr-hydroxides) dissolved in the hexane. According to UV–vis spectra, the two samples showed similar absorption property beyond 250 nm, which is a broad band at 300 nm related with the $O^{2-} \rightarrow Ce^{4+}$ charge transfer (CT)

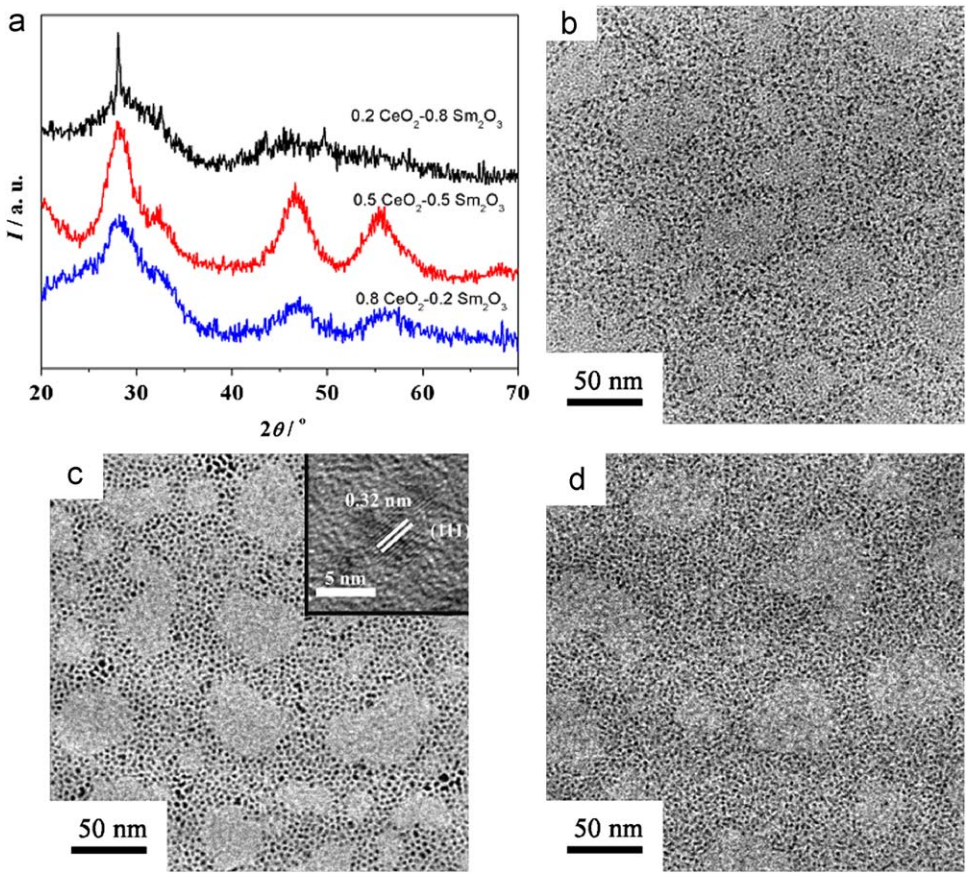

Fig. 6. (a) PXRD of the as-prepared $Ce_{1-x}Sm_xO_{1-x/2}$ ($x = 0.2, 0.5, 0.8$) nanocrystals; TEM images of the as-prepared $Ce_{1-x}Sm_xO_{1-x/2}$ ($x = 0.2, 0.5, 0.8$) nanocrystals: (b) $x = 0.2$, 1 mmol (Ce,Sm)-hydroxides, OA/OM = 2:3, 300 °C, 1 h; (c) $x = 0.5$, 1 mmol (Ce,Sm)-hydroxides, OA/OM = 1:3, 300 °C, 1 h; (d) $x = 0.8$, 1 mmol (Ce,Sm)-hydroxides, OA/OM = 1:3, 300 °C, 1 h.

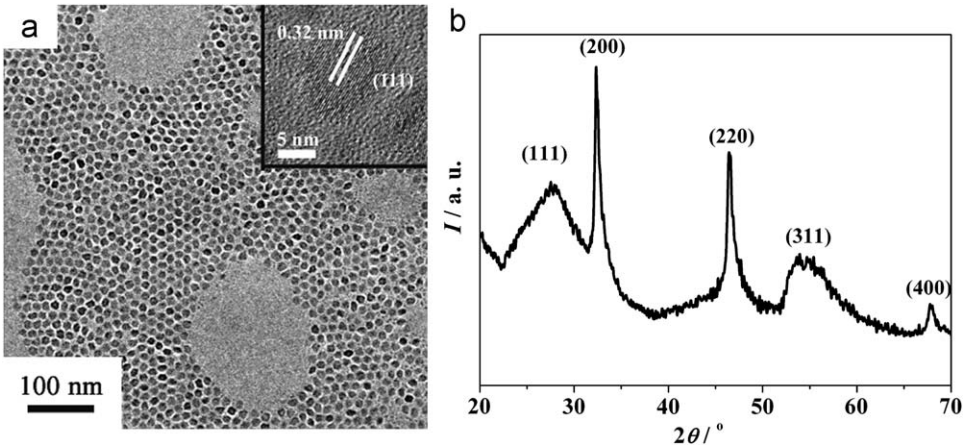

Fig. 7. (a) TEM images and (b) PXRD of the as-prepared $Ce_{0.5}Sm_{0.5}O_{1.75}$ nanocrystals, with 1 mmol (Ce,Sm)-hydroxides, OA/OM = 2:3, 300 °C, 1 h, where the (Ce,Sm)-hydroxides obtained from the $(NH_4)_2Ce(NO_3)_6$ and $SmCl_3$.

transitions. With respect to the absorption lower than 250 nm, the (Ce,Zr)-hydroxides showed absorption at 233 nm, while the absorption of the separate counterparts (Ce-hydroxides mixed with Zr-hydroxides) is at 220 nm. The difference can be probably ascribed to the bond-linkage or interaction between Ce^{4+} and Zr^{4+} in the (Ce,Zr)-hydroxides precursor, whose UV–vis absorption behavior is similar to that of the as-prepared CeO_2–ZrO_2 products, shown in Fig. 2. Therefore, we conclude that highly homogeneous co-mixture during the formation of hydrated (Ce,Zr)-hydroxides precursor is the key factor for the formation of $Ce_{1-x}Zr_xO_2$ solid solutions with good stoichiometric homogeneity in a wide range of Ce/Zr ratios.

3.3. Controllable synthesis of other rare-earth-based solid solutions

Doped ceria is an important material because of its potential applications in solid electrolyte used in oxygen concentration cells and in solid oxide fuel cells. It is also a candidate material for application in controlling air-to-fuel ratio in automobile exhaust

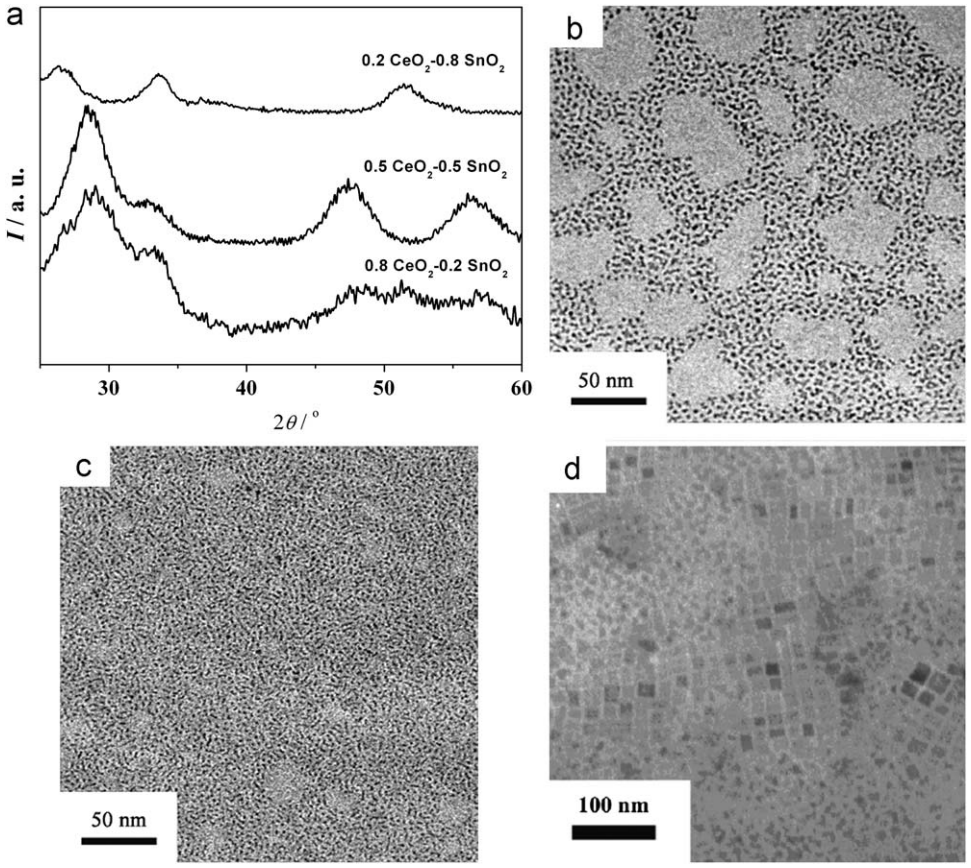

Fig. 8. (a) PXRD of the as-prepared $Ce_{1-x}Sn_xO_2$ ($x = 0.2$, 0.5, 0.8) nanocrystals; TEM images of the as-prepared $Ce_{1-x}Sn_xO_2$ ($x = 0.2$, 0.5, 0.8) nanocrystals: (b) $x = 0.2$, 1 mmol (Ce,Sn)-hydroxides, OA/OM = 1:3, 300 °C, 0.5 h; (c) $x = 0.5$, 1 mmol (Ce,Sn)-hydroxides, OA/OM = 2:3, 300 °C, 0.5 h; (d) $x = 0.8$, 1 mmol (Ce,Sn)-hydroxides, OA/OM = 2:3, 300 °C, 0.5 h.

[51]. Aliovalent substitution of trivalent rare-earth ions in ceria leads to the creation of oxide ion vacancies giving rise to increase in ionic conductivity. Among the trivalent rare-earth-doped ceria, the highest conductivities are observed in $Ce_{1-x}Gd_xO_{2-x/2}$ and $Ce_{1-x}Sm_xO_{2-x/2}$ [13,14]. While for the quadrivalent substitution, Ce–Sn solid solutions are the important catalysts for their superior redox efficiency at low temperature [15]. Therefore, the synthesis of doped ceria solid solutions mentioned above with better textural property, thermal stability, and redox or ion conductivity behaviors becomes the hotspot in synthetic chemistry. To date, $Ce_{1-x}Gd_xO_{2-x/2}$, $Ce_{1-x}Sm_xO_{2-x/2}$, and $Ce_{1-x}Sn_xO_2$ solid solutions were usually obtained through the methods including co-precipitation, high-temperature milling, etc. [27–29]. The resulting products display broad size distribution, ranging from bulk to nanomaterials, irregular morphology and bad dispersability. Fortunately, the present synthesis strategy can be successfully extended to the formation of other rare-earth-based solid solutions, such as $Ce_{1-x}Gd_xO_{2-x/2}$, $Ce_{1-x}Sm_xO_{2-x/2}$, and $Ce_{1-x}Sn_xO_2$.

3.3.1. $Ce_{1-x}Gd_xO_{2-x/2}$

PXRD patterns of the as-prepared $Ce_{1-x}Gd_xO_{2-x/2}$ ($x = 0.2$, 0.5, 0.8) nanocrystals are shown in Fig. 5a. The broadening of the reflections in the diffractograms distinctly indicates their ultra-small size. The peaks' shift to low angle with x, increasing from 0.2 to 0.5, confirms the formation of solid solution. However, when x is increased to 0.8, a slight sharp peak appeared at 28.4°, probably indicating the separation of ceria and gadolinia. Lattice constant for $Ce_{0.8}Gd_{0.2}O_{1.9}$ is $a = 5.4248(0)$ Å, and is comparable to the value of the JCPDS card (no. 75–0162), which is 5.423 Å. The typical TEM micrographs of the as-prepared $Ce_{1-x}Gd_xO_{1-x/2}$ ($x = 0.2$, 0.5, 0.8) nanocrystals are shown in Fig. 5b–d. Similar to the $Ce_{1-x}Zr_xO_2$ nanocrystals, $Ce_{1-x}Gd_xO_{1-x/2}$ also exhibits ultra-small size, which are 4.4 nm ± 0.6 nm, 3.2 nm ± 0.4 nm for $Ce_{0.8}Gd_{0.2}O_{1.9}$ and $Ce_{0.5}Gd_{0.5}O_{1.75}$, respectively. Taking $Ce_{0.5}Gd_{0.5}O_{1.75}$ as a representative example, we found that the lattice fringes with the interplanar spacing of 0.32 nm (see the inset of Fig. 5c) were determined to be associated with the {111} facets of $Ce_{0.5}Gd_{0.5}O_{1.75}$. In addition, the EDAX results for $Ce_{0.5}Gd_{0.5}O_{1.75}$ shown in Table 1 further proved the homogenous texture.

3.3.2. $Ce_{1-x}Sm_xO_{2-x/2}$

Similarly, three compositions of $Ce_{1-x}Sm_xO_{1-x/2}$ ($x = 0.2$, 0.5, 0.8) were synthesized in the CeO_2–Sm_2O_3 system. Typical XRD patterns belonging to this series are shown in Fig. 6a. On doping 20% Sm_2O_3 into CeO_2, the structure $Ce_{0.8}Sm_{0.2}O_{1.9}$ becomes a cubic fluorite structure. It is convincing to deduce that the structures of both $Ce_{0.8}Sm_{0.2}O_{1.9}$ and $Ce_{0.5}Sm_{0.5}O_{1.75}$ are homogeneous cubic fluorite structure, for which their peaks shift to low angle regularly with the increased replacement of Ce^{4+} ions by larger Sm^{3+} ones. When $x = 0.8$, sharp peaks co-existed with broad peaks in the PXRD pattern, evincing the phase separation, which forms both ceria and samaria. Lattice constant for the $Ce_{0.8}Sm_{0.2}O_{1.9}$ is 5.4413 (5) Å, to be compared with the value of the JCPDS card (no. 75–0158), which is 5.433 Å. As shown in Fig. 6b and c, typical TEM micrographs of the as-prepared $Ce_{1-x}Sm_xO_{1-x/2}$ ($x = 0.2$, 0.5) nanocrystals exhibited ultra-small size, that is 3.6 nm ± 0.3 nm and 3.2 nm ± 0.6 nm for $Ce_{0.8}Sm_{0.2}O_{1.9}$

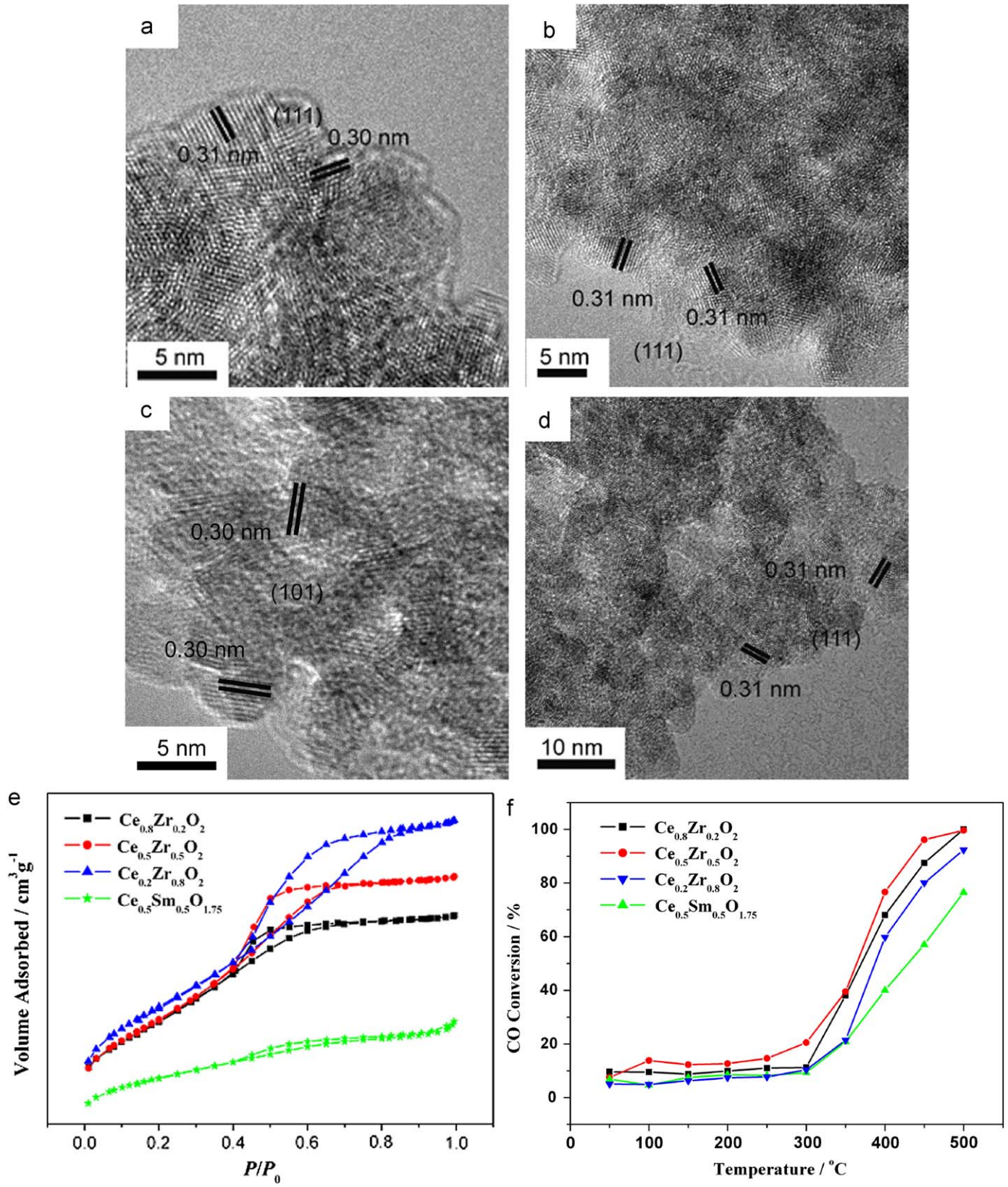

Fig. 9. TEM images of the as-prepared $Ce_{1-x}Zr_xO_2$ ($x = 0.2$, 0.5, 0.8) catalysts: (a) $x = 0.2$; (b) $x = 0.5$; (c) $x = 0.8$; (d) TEM images of the as-prepared $Ce_{0.5}Sm_{0.5}O_{1.75}$ catalysts; (e) N_2 adsorption–desorption isotherms of the ceria-based catalysts at 400 °C for 4 h in still air; (f) CO conversion percent vs. reaction temperature for the ceria-based catalysts.

and $Ce_{0.5}Sm_{0.5}O_{1.75}$, respectively. $Ce_{0.5}Sm_{0.5}O_{1.75}$ showed lattice fringes with interplanar spacing of 0.32 nm associated with the (111) facets of $Ce_{0.5}Sm_{0.5}O_{1.75}$ in the inset of Fig. 6c.

More interestingly, when $SmCl_3$ replaced $Sm(NO_3)_3$ as the starting material, the morphology and size (Fig. 7a) of the resulting products were quite different. The Bragg reflections

shown in the PXRD patterns of Fig. 7b can be attributed to a cubic fluorite structure, with the calculated lattice constants of $a = 5.5609(9)$ Å for the $Ce_{0.5}Sm_{0.5}O_2$ nanocrystals. Furthermore, the peaks in 27.6° and 54.2° seem to be quite broad, while those in 32.3°, 46.5°, and 67.9° are sharp, probably suggesting that the nanocrystals grow epitaxially. The lattice fringes with the interplanar spacing of 0.32 nm in the inset of Fig. 7a were determined to be associated with the (111) facets of $Ce_{0.5}Sm_{0.5}O_2$, which further proved that the nanocrystals were inclined to grow along [100] or [110]. EDAX results showed that the obtained $Ce_{0.5}Sm_{0.5}O_2$ sample exhibited a homogenous texture.

3.3.3. $Ce_{1-x}Sn_xO_2$

The presented synthesis strategy has been attempted for the preparation of $Ce_{1-x}Sn_xO_2$ ($x = 0.2$, 0.5, 0.8). Fig. 8a shows the PXRD patterns of $Ce_{1-x}Sn_xO_2$ with different Sn doping concentrations. When $x = 0.2$ or 0.5, the broadening of the reflections and peak shifting probably mean the possible formation of ultra-small $Ce_{1-x}Sn_xO_2$ solid solutions; whereas when x increased to 0.8, the typical SnO_2 phase, tetragonal-structure features in the diffraction pattern appear. Corresponding to the TEM (Fig. 8) coupled with EDAX analysis (Table 1), the $Ce_{1-x}Sn_xO_2$ ($x = 0.2$, 0.5) shows homogenous texture with the size of 3.3 nm ± 0.6 nm and 3.0 nm ± 0.4 nm, respectively. While in $x = 0.8$, the nanopolyhedra presenting the ceria and nanocubes correlating to tin oxide co-existed in the TEM images.

3.4. Catalytic activity of CeO_2–ZrO_2 solid solutions for CO oxidization

CO oxidization reaction was selected to test the catalytic activity of the as-obtained $Ce_{1-x}Zr_xO_2$ ($x = 0.2$, 0.5, 0.8) and $Ce_{1-x}Sm_xO_{2-x/2}$ ($x = 0.5$). The catalysts were obtained by calcination at 400 °C for 4 h in air. Because of the ultra-small size of the nanocrystals, together with the violent removal of the capping ligands by the calcination treatment, the as-calcined nanocrystals are highly porous (Fig. 9) and show a large BET specific surface area of 209, 199, and 233 $m^2 g^{-1}$ for the $Ce_{1-x}Zr_xO_2$ ($x = 0.2$, 0.5, and 0.8), respectively, much higher than that of the CeO_2–ZrO_2 materials prepared by hydrothermal synthesis (104–184 $m^2 g^{-1}$) [19], and 104 $m^2 g^{-1}$ for $Ce_{0.5}Sm_{0.5}O_{1.75}$. The introduction of ZrO_2 to CeO_2 markedly improved the surface areas of as-calcined samples, possibly due to the inhibition of grain growth and fusion of the as-prepared nanocrystals during the high-temperature sintering process.

Fig. 9f shows the plot of CO conversion percentage versus reaction temperature for the $Ce_{1-x}Zr_xO_2$ and $Ce_{0.5}Sm_{0.5}O_{1.75}$ catalysts. To convert CO to CO_2 from 200 to 500 °C, for T_{50} (50% CO conversion temperature), the temperature for starting activity of the catalysts is found to follow the sequence of $Ce_{0.5}Zr_{0.5}O_2 > Ce_{0.8}Zr_{0.2}O_2 > Ce_{0.2}Zr_{0.8}O_2 > Ce_{0.5}Sm_{0.5}O_{1.75}$. It has been found that there is a weak relationship between the particle sizes D or surface area S and the CO conversion of the present nanocrystals, indicating that the external texture is not the key factor affecting the CO conversion ability of the present $Ce_{1-x}Zr_xO_2$ solid solutions. The CO conversion activity of the present catalysts shows similarity with the OSC value of the hydrothermal products reported by our group [4], which correlates with the lattice strain of the CeO_2–ZrO_2 catalyst. In the current work, the optimal zirconium content x for our $Ce_{1-x}Zr_xO_2$ catalysts was 0.5. Furthermore, the CO conversion activity of $Ce_{0.5}Sm_{0.5}O_{1.75}$ was worse than that of $Ce_{1-x}Zr_xO_2$ ($x = 0.2$, 0.5, 0.8), indicating that ZrO_2 is a beneficial dopant rather than Sm_2O_3 in CO oxidization reaction.

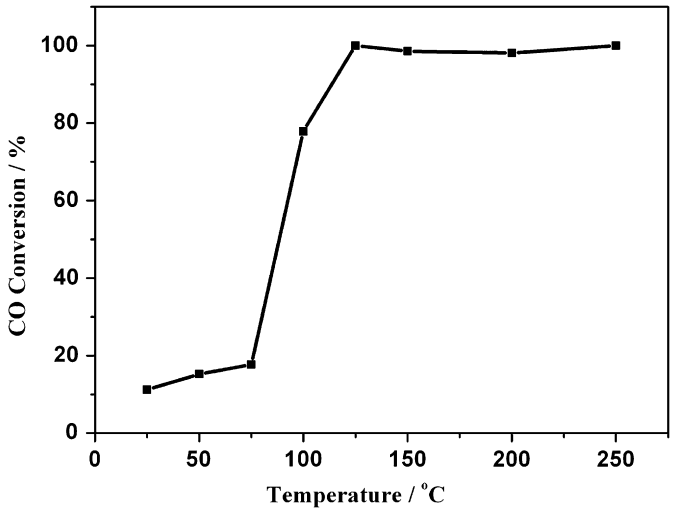

Fig. 10. Catalytic activity of $Pt/Ce_{0.5}Zr_{0.5}O_2$ for CO oxidation.

The $Ce_{1-x}Zr_xO_2$ solid solutions have proven to be ideal catalyst supports. However, their CO conversion relates both to the nanostructure and to the adopted experimental conditions. In this work, the best catalyst $Ce_{0.5}Zr_{0.5}O_2$ was loaded with 3 wt% of 3 nm Pt nanoparticles and then was employed to test CO oxidation. The evolution of CO conversion as a function of temperature is presented in Fig. 10. It shows that the as-prepared $Pt/Ce_{0.5}Zr_{0.5}O_2$ catalyst possesses high CO oxidation activity, that is, almost 80% and 100% conversions at temperatures of 100 and 125 °C are observed.

In addition, BET measurement of samples calcined at an elevated temperature was carried out to investigate the thermal stability. The $Ce_{0.5}Zr_{0.5}O_2$ sample calcined at 900 °C shows a smaller BET area (33.5 $m^2 g^{-1}$) compared to that calcined at 400 °C (with a BET surface area of 199 $m^2 g^{-1}$), probably owing to the larger extent of particle agglomeration at higher temperatures. However, the decreased BET surface area is still much larger than that (0.62 $m^2 g^{-1}$) of the bulk ceria calcined at 1000 °C, reported by our previous work [52]. We considered that the system could partially preserve their nature up to 900 °C. Moreover, CO oxidization reaction was also selected to test the stability of $Ce_{0.5}Zr_{0.5}O_2$, which was calcined at 400 °C for 4 h in still air. After one cycle, no loss of catalytic activity was observed. Therefore, these results strongly suggest that the $Ce_{1-x}Zr_xO_2$ solid solutions could serve as excellent catalysts in various fields.

4. Conclusion

CeO_2–ZrO_2 solid solutions with various Ce/Zr ratios have been successfully obtained via a facile method including the initial formation of (Ce,Zr)-hydroxides at low temperature and the thermolysis process at high temperature. The characterizations of TEM, EDAX, PXRD, Raman, and UV–vis absorption have proved that the CeO_2–ZrO_2 solid solutions have a homogenous texture and good thermal stability. The dopant of ZrO_2 can increase the ratios of Ce^{3+} to Ce^{4+} in the nanoparticles, thus improving the CO conversion catalytic property. In addition, the present strategy was extended to the synthesis of CeO_2–Sm_2O_3, CeO_2–Gd_2O_3, and CeO_2–SnO_2 solid solutions with a homogeneous texture. These high-quality nanocrystals are easy to disperse in the non-polar solvents and assemble into large-area films. It is expected that this facile method can be applied to synthesize other ultra-small and uniform solid solutions, which may serve as the candidate for

nanostructured catalysis, via the bottom-up approach based on nanocrystal self-assembly.

Acknowledgements

We gratefully acknowledge the financial aids from the MOST of China (Grant no. 2006CB601104) and the NSFC (Grant nos. 20871006, 20821091, and 20671005).

References

[1] A. Trovarelli, Catalysis by Ceria and Related Materials, 2nd ed., Dunod, London, 2002.
[2] B.R. Powell, R.L. Bloink, C.C. Eickel, J. Am. Ceram. Soc. 71 (1988) 104.
[3] J. Kašpar, P. Fornasiero, M. raziani, Catal. Today 50 (1999) 285.
[4] R. Si, Y.W. Zhang, S.J. Li, B.X. Lin, C.H. Yan, J. Phys. Chem. B 108 (2004) 12481.
[5] B.C.H. Steele, Nature (London) 400 (1999) 619.
[6] A. Atkinson, S. Barnett, R.J. Gorte, J.T.S. Irvine, A.J. Mcevoy, M. Mogensen, S.C. Singhal, J. Vohs, Nat. Mater. 3 (2004) 17.
[7] E. Mamontov, T. Egami, R. Brezny, M. Koranne, S. Tyagi, J. Phys. Chem. B 104 (2000) 11110.
[8] T. Masui, K. Fujiwara, K.I. Machida, G.Y. Adachi, Chem. Mater. 9 (1997) 2197.
[9] Y.W. Zhang, R. Si, C.S. Liao, C.H. Yan, C.X. Xiao, Y. Kou, J. Phys. Chem. B 107 (2003) 10159.
[10] Q. Fu, H. Saltsburg, M. Flytzani-Stephanopoulos, Science 301 (2003) 935.
[11] P. Fornasiero, G. Balducci, R. Di Monte, J. Kašpar, V. Sergo, G. Gubitosa, A. Ferrero, M. Graziani, J. Catal. 164 (1996) 173.
[12] J. Kašpar, P. Fornasiero, N. Hickey, Catal. Today 77 (2003) 419.
[13] H. Yahiro, Y. Eguchi, K. Eguchi, H. Arai, J. Appl. Electrochem. 18 (1988) 527.
[14] B.C.H. Steele, in: T. Takahashi (Ed.), High Conductivity Solid Ionic Conductors, Recent Trends and Applications, World Scientific, London, 1989, p. 402.
[15] R. Sasikala, N.M. Gupta, S.K. Kulshreshtha, Catal. Lett. 71 (2001) 69.
[16] C. De Leitenburg, A. Trovarelli, F. Zamar, S. Maschio, G. Dolcetti, J. Llorca, J. Chem. Soc. Chem. Commun. (1995) 2181.
[17] M. Hirano, T. Miwa, M. Inagaki, J. Solid State Chem. 158 (2001) 112.
[18] S. Rossignol, F. Gérard, D. Duprez, J. Mater. Chem. 9 (1999) 1615.
[19] A. Cabanas, J.A. Darr, E. Lester, M. Poliakoff, J. Mater. Chem. 11 (2001) 561.
[20] Q. Yuan, Q. Liu, W.G. Song, W. Feng, W.L. Pu, L.D. Sun, Y.W. Zhang, C.H. Yan, J. Am. Chem. Soc. 129 (2007) 6698.
[21] X. Liang, X. Wang, Y. Zhuang, B. Xu, S.M. Kuang, Y.D. Li, J. Am. Chem. Soc. 130 (2008) 2736.
[22] T. Taniguchi, T. Watanabe, N. Sakamoto, N. Matsushita, M. Yoshimura, Cryst. Growth Des. 8 (2008) 3725.
[23] A. Ahniyaz, T. Fujiwara, T. Fujino, M. Yoshimura, J. Nanosci. Nanotechnol. 4 (2004) 233.
[24] A.S. Deshpande, N. Pinna, P. Beato, M. Antonietti, M. Niederberger, Chem. Mater. 16 (2004) 2599.
[25] S. Pengpanich, V. Meeyoo, T. Rirksomboon, K. Bunyakiat, Appl. Catal. A: Gen. 234 (2002) 221.
[26] J. Kašpar, P. Fornasiero, J. Solid State Chem. 171 (2003) 19.
[27] C. Peng, Y. Wang, K. Jiang, B.Q. Bin, H.W. Liang, J. Feng, J. Meng, J. Alloys Compd. 349 (2003) 273.
[28] T.B. Nguyen, J.P. Deloume, V. Perrichon, Appl. Catal. A: Gen. 249 (2003) 273.
[29] G. Chiodelli, L. Malavasi, V. Massarotti, P. Mustarelli, E. Quartarone, Solid State Ionics 176 (2005) 1505.
[30] T. Teranishi, M. Hosoe, T. Tanaka, M. Miyake, J. Phys. Chem. B 103 (1999) 3818.
[31] S.W. Yang, L. Gao, J. Am. Chem. Soc. 128 (2006) 9330.
[32] T.Y. Yu, J. Joo, Y.I. Park, T. Hyeon, Angew. Chem. Int. Ed. 44 (2005) 7411.
[33] H. Gu, M.D. Soucek, Chem. Mater. 19 (2007) 1103.
[34] J. Joo, T. Yu, Y.W. Kim, H.M. Park, F.X. Wu, J.Z. Zhang, T. Hyeon, J. Am. Chem. Soc. 125 (2003) 6553.
[35] G. Garnweitner, L.M. Goldenberg, O.V. Sakhno, M. Antonietti, M. Niederberger, J. Stumpe, Small 3 (2007) 1626.
[36] R. Si, Y.W. Zhang, L.P. You, C.H. Yan, Angew. Chem. Int. Ed. 44 (2005) 3256.
[37] Z.C. Orel, B. Orel, Phys. Status Solidi B 186 (1994) K33.
[38] G.R. Rao, H.R. Sahu, Proc. Indian Acad. Sci. (Chem. Sci.) 113 (2001) 651.
[39] M. Yashima, K. Morimoto, N. Ishizawa, M. Yoshimura, J. Am. Ceram. Soc. 76 (1993) 1745.
[40] M. Yashima, K. Morimoto, N. Ishizawa, M. Yoshimura, J. Am. Ceram. Soc. 76 (1993) 2865.
[41] M. Yashima, H. Arashi, M. Kakihana, M. Yoshimura, J. Am. Ceram. Soc. 77 (1994) 1067.
[42] M. Yashima, K. Ohtake, M. Kakihana, M. Yoshimura, J. Am. Ceram. Soc. 76 (1993) 2773.
[43] A. Martínez-Arias, M. Fernández-García, V. Ballesteros, L.N. Salamanca, J.C. Conesa, C. Otero, J. Soria, Langmuir 15 (1999) 4796.
[44] E.F. López, V.S. Escribano, M. Panizza, M.M. Carnasciali, G. Busca, J. Mater. Chem. 11 (2001) 1891.
[45] J.R. McBride, K.C. Hass, B.D. Poindexter, W.H. Weber, J. Appl. Phys. 76 (1994) 2435.
[46] P. Fornasiero, A. Speghini, R.D. Monte, M. Bettinelli, J. Kašpar, A. Bigotto, V. Sergo, M. Graziani, Chem. Mater. 16 (2004) 1938.
[47] J. Kašpar, R. Di Monte, P. Fornasiero, M. Graziani, H. Bradshaw, C. Norman, Top. Catal. 16–17 (2001) 83.
[48] R. Si, Y.W. Zhang, H.P. Zhou, L.D. Sun, C.H. Yan, Chem. Mater. 1 (2007) 18.
[49] H.X. Mai, Y.W. Zhang, L.D. Sun, C.H. Yan, Chem. Mater. 19 (2007) 4514.
[50] J.D. Lin, J.G. Duh, J. Am. Ceram. Soc. 80 (1997) 92.
[51] E. M. Logothetis, in: Proceedings of the 12th State of-the-art Symposium on Ceramics in Service of Men, Washington, DC, 1976.
[52] H.P. Zhou, Y.W. Zhang, R. Si, L.-S. Zhang, W.G. Song, C.H. Yan, J. Phys. Chem. C 112 (2008) 20366.